Light: Science & Applications (2017) 6, e17072; doi:10.1038/lsa.2017.72
Official journal of the CIOMP 2047-7538/17
www.nature.com/lsa

ORIGINAL ARTICLE

Phase-controlled propagation of surface plasmons

Basudeb Sain*, Roy Kaner* and Yehiam Prior

Directional emission of electromagnetic radiation can be achieved using a properly shaped single antenna or a phased array of individual antennas. Control of the individual phases within an array enables scanning or other manipulations of the emission, and it is this property of phased arrays that makes them attractive in modern systems. Likewise, the propagation of surface plasmons at the interface between metal films and dielectric materials can be determined by shaping the individual surface nanostructures or via the phase control of individual elements in an array of such structures. Here, we demonstrate control of the propagation of surface plasmons within a linear array of nanostructures. The generic situation of plasmonic surface propagation that is different on both sides of a metal film provides a unique opportunity for such control: plasmons propagating on the slower side feed into the side with the faster propagation, creating a phased array of interfering antennas and thus controlling the directionality of the wake fields. We further show that by shaping the individual nanoantennas, we can generate an asymmetric propagation geometry.
Light: Science & Applications (2017) **6,** e17072; doi:10.1038/lsa.2017.72; published online 20 October 2017

Keywords: FDTD; NSOM; phased array; plasmonic wakes; surface plasmons

INTRODUCTION

Surface Plasmon Polaritons (SPPs) are promising candidates for the next generation of photonic circuits. Similar to photons, they can carry information; they are directional and coherent, and they have the advantage of occupying a space much smaller than the diffraction limit of light. Because of this, much effort has been made to control the directionality of SPPs. In particular, there has been a focus on creating small plasmonic devices that can efficiently couple light to SPPs and guide them to regions of interest.

These plasmonic structures include gratings, ridge-grating structures[1] and slits[2], which are parallel for directing or curved for focusing. Some devices use an asymmetric geometry to achieve directionality, such as aperiodic grooves[3,4], asymmetric nanoslits[5,6] and tilted gratings[7,8]. Many of the devices utilized relative phase control to route plasmons. The idea is to use multiple radiation sources with phase discontinuities, the sum of which creates directional SPPs. Generally, there are two main mechanisms of creating phase discontinuities. One is the use of a phased array antenna[9], in which each radiation source is driven at the same frequency, but with a slight phase shift toward its neighbors. This is very common in radio frequencies and is also used for microwaves[10] and optics[11,12]. The other mechanism is holography, in which each of the antennas is excited with the same frequency and phase, but due to the different response engineered for each antenna, a phase shift is created.

The holography mechanism is vastly used in plasmonics. For example, it has been used to couple light to SPPs with specific directionality by using two compact detuned antennas[13], each reacting differently to the incoming light, or by using arrays of grooves with different alignments[14] or positions[15] on a metallic surface. Holography has even been used to create plasmonic airy beams[16]. It has also been used to steer far-field light in the linear[17,18] and nonlinear regimes[19]. Lately, it has also been used by Genevet *et al*[20]. to create plasmonic wake fields. Prior to that work, the creation of plasmonic optical wake fields was demonstrated only by using the Smith–Purcell effect[21], in which wake fields are created due to the passing of a charged particle nearby a grating, an effect that has been demonstrated in photonic crystals[22] and is enhanced in plasmonic systems[23]. On the other hand, hardly any work has been reported regarding directional SPPs using a plasmonic phased array.

Our scheme is based on the polarization-dependent[24] coupling of nanocavities by propagating plasmons. We excite a single cavity, and the energy is carried from that point to the other antennas by SPPs[25,26] over a 1D array[2]. Using this method, only a very small structure (spot) needs to be illuminated, and one can couple light efficiently to directional SPPs; thus, the excitation can even be done using fiber optics. In addition, the direction of the outgoing SPPs is independent of the angle of illumination, making this method very robust.

MATERIALS AND METHODS

The experimental system consists of a thin gold film, in which a linear array of nanocavities is fabricated with varying cavity spacing. The metal film is deposited on a glass substrate so that the surface plasmons above and below the film propagate at different velocities. A linearly polarized laser beam at 632.8 nm (HeNe) was focused from the glass-side on the first cavity of the array, and the near field above the cavities was measured[27] by using a Near-field Scanning Optical Microscope (NSOM; Nanonics Imaging Ltd. Multiview 4000;

Department of Chemical Physics, Weizmann Institute of Science, Rehovot 76100, Israel
*These authors contributed equally to this work.
Correspondence: Y Prior, Email: yehiam.prior@weizmann.ac.il
Received 27 November 2016; revised 18 April 2017; accepted 21 April 2017; accepted article preview online 24 April 2017

Figure 1a). The propagation of the SPPs was set to be along the array by adjusting the laser polarization.

In the NSOM measurements[28] we used a tapered optical fiber, coated with metal (Cr/Au in this work) and mounted on a tuning fork (Figure 1c). In the aperture NSOM method, the background is almost negligible because the signal is collected through the optical fiber (here, a multimode fiber), which is positioned a few tens of nanometers above the surface, and the light reaches the APD single photon detector (Excelitas SPCM-AQRH-14-24504) directly, the scanning software of which produces the NSOM image. The bending of the tip(≈30° between the tip apex and the sample surface normal) enables the detection of the normal force in the tuning fork feedback. The tips were cut by using Focused Ion Beam (FIB) for better accuracy of the aperture size and shape (Figure 1c) and for the tip surface to be parallel to the sample surface. As a tradeoff between higher spatial resolution (smaller tip size) and higher signal levels, we selected 100 nm tips with a maximum laser power of 10 mW.

Gold films of typical thickness (350 nm) were e-beam evaporated on thoroughly cleaned 300 micron-thick borosilicate glass slides (Waldemar Knittel Glasberbeitungs GmbH). Linear arrays of rectangular nanocavities with individual dimensions of 100×500 nm (Figure 1b), with different lattice constants, were milled by using a FIB (FEI, Helios Nano Lab 600i) with a Ga ion and electron source. The thickness of 350 nm was chosen so that the transmission of the red light through the gold film would be very low.

Detailed numerical simulations of the fields above and below the sample were performed by means of the finite-difference time-domain (FDTD) method using the commercial Lumerical Numerical Solutions package[29]. The optical constants of gold were taken from Johnson and Christy[30], while the optical constants of SiO_2 were taken from Palik[31]. The light source was a plane wave, polarized along the axis of the array (x-axis) traveling in the z direction perpendicular to the plane of the film. To compare the results with the NSOM measurement, the magnitude of the electric field, $|\mathbf{E}|^2$, was calculated at a height of 50 nm above the gold film.

In addition to the numerical simulations, and to gain a better physical understanding of the results, we developed a simplified physical model based on the uncoupled source point approximation. Independent dipoles were assumed to be located on the edge of each rectangular nanocavity, each one modeled as a source point radiating at the same frequency, as determined based on the excitation light. The amplitude and phase of each source point were as if the source point was excited by an uninterrupted propagating plasmon. Therefore, the amplitude is only a function of the distance from the excitation hole and the plasmon decay length, whereas the phase is a function of the distance from the excitation hole and the plasmon wavelength, both of which are properties of the metal and the interface.

RESULTS AND DISCUSSION

Figure 2 depicts the simulated and calculated results of the near field excited above a gold film under two different conditions: as a free-standing film with air on both sides, and as a thin film deposited on a glass substrate. The differences are pronounced. For the free-standing film (Figure 2a), the illuminated cavity radiates a dipole emission in both the right and left directions, with uninterrupted propagation to the left and with propagation to the right that is disturbed by the other cavities, namely, the simple dipole pattern is locally affected by interference from the individual cavities. In Figure 2b, the situation is very different: while the radiation to the left is similar, very prominent side lobes are generated to the right. The origin of these side lobes, which appear as propagating wakes, is the main focus of the present work. The model calculations (Figure 2c and 2d) show qualitatively equivalent results—a simple uninterrupted propagation for the free standing film and the generation of side lobes for the air/gold/glass configuration.

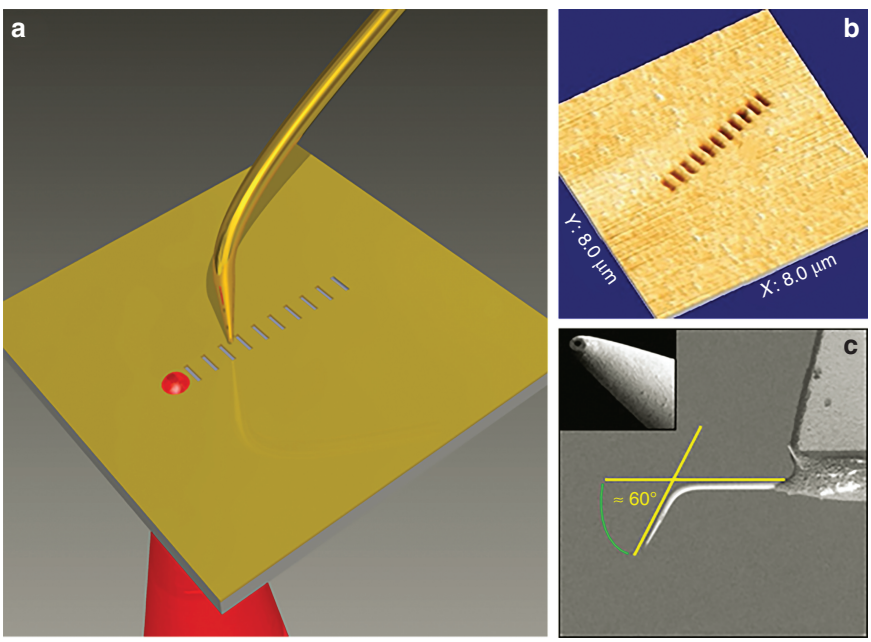

Figure 1 Experimental configuration. (**a**) Artist's view of the arrangement. A laser beam illuminates the first cavity from below, and the excited field above the gold film is measured using the NSOM probe. (**b**) SEM image of a one-dimensional array of eleven rectangular nanocavities of dimensions 100×500 nm with a 300 nm gap milled in a high-quality gold film 350 nm thick. The topography was measured simultaneously with the near-field measurements using the same NSOM probe. (**c**) SEM image of Nanonics NSOM tip showing the bending of the tip and its connection to one arm of the tuning fork. The inset shows the tip after cutting its apex using the Focused Ion Beam (see text for details).

doi:10.1038/lsa.2017.72

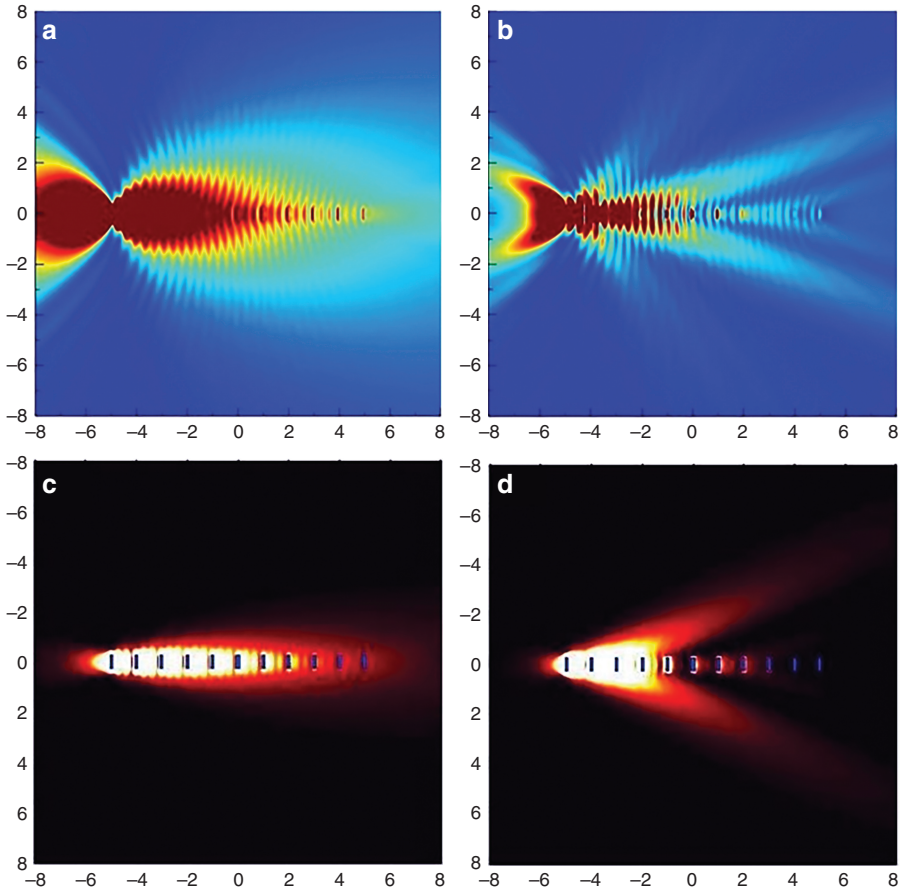

Figure 2 Near field above a gold film. (**a**) Simulated near field above a free-standing film (air on both sides) for excitation of the first cavity by a HeNe laser beam. (**b**) The same as in (**a**) but for a gold film that is deposited on a glass substrate. Field distributions calculated by the simplified model for the free-standing film (**c**) and for the air/gold/glass film (**d**) (see text for details).

The physical explanation for these side lobes, which is elaborated below, is as follows: the laser excitation of the first cavity generates two propagating plasmons: one at the gold–air interface and one at the gold–glass interface. These two surface plasmons propagate at different velocities, with the one at the gold–glass interface being slower. This slower wave propagates through the other cavities, feeding into the upper surface at each one. Due to the velocity difference between the two propagating plasmons, phase retardation (phase array of the emitters) is created, which is felt by the plasmon propagating on the gold–air surface. Like with any phase antenna, scattering of the side lobes is generated with angles that depend on the location and phase of the other cavities. In the following section, we investigate this phenomenon experimentally and analyze the observations by numerically solving the wave equations and by using our conceptual model, which is based on placing a properly phased radiating dipole in each cavity.

The side lobes are generated differently for arrays with different gaps between the cavities. Figure 3 depicts some typical results. At the 300 nm gap, the lobes spread from each individual nanocavity in a direction that is almost perpendicular to the array axis. At larger gaps, various branches are seen in the propagation, with two dominant lobes evolving at larger gaps. As a general observation, two dominant side lobes propagate at angles that vary with the gap between the antennas, with additional, less pronounced, lobes that seem to originate at every individual scattering cavity. The propagation to the free space on the left side is hardly affected. Overall, what is observed is the scattering from a phase array of antennas whose phase delay is dictated by the gold–glass plasmon and the gap between the cavities.

In Figure 4, the simulated results for the same set of arrays are shown. While the numerical simulations are expected to capture the qualitative nature of the physical observations, they cannot be expected to yield quantitative agreement with the measured results. The dimensions of the fabricated cavities are not exactly as designed, the sharpness of the facets and corners is not perfect (as is assumed in the simulations), surface imperfections are not accounted for, metal grains and layer thickness fluctuations are ignored, and several other such 'technical' imperfections are found to affect the details of the simulated results.

The refractive index of the glass determines the plasmon propagation velocity at the gold–glass interface. To characterize this effect, the scattering from an array of cavities with a gap of 900 nm is simulated for different substrate refractive indices between 1.0 and 2.0, and significant differences between them are found (Figure 5). This strong dependence on the refractive index is the origin of the proposal to use variable index interfaces to control the side-lobe propagation, as described below.

As mentioned, to elucidate the physical picture, we developed a simplified model to explain the results. Individual dipoles are placed around each nanocavity location, with intensity defined based on the decaying 'top' plasmon and the phase defined according to the arrival

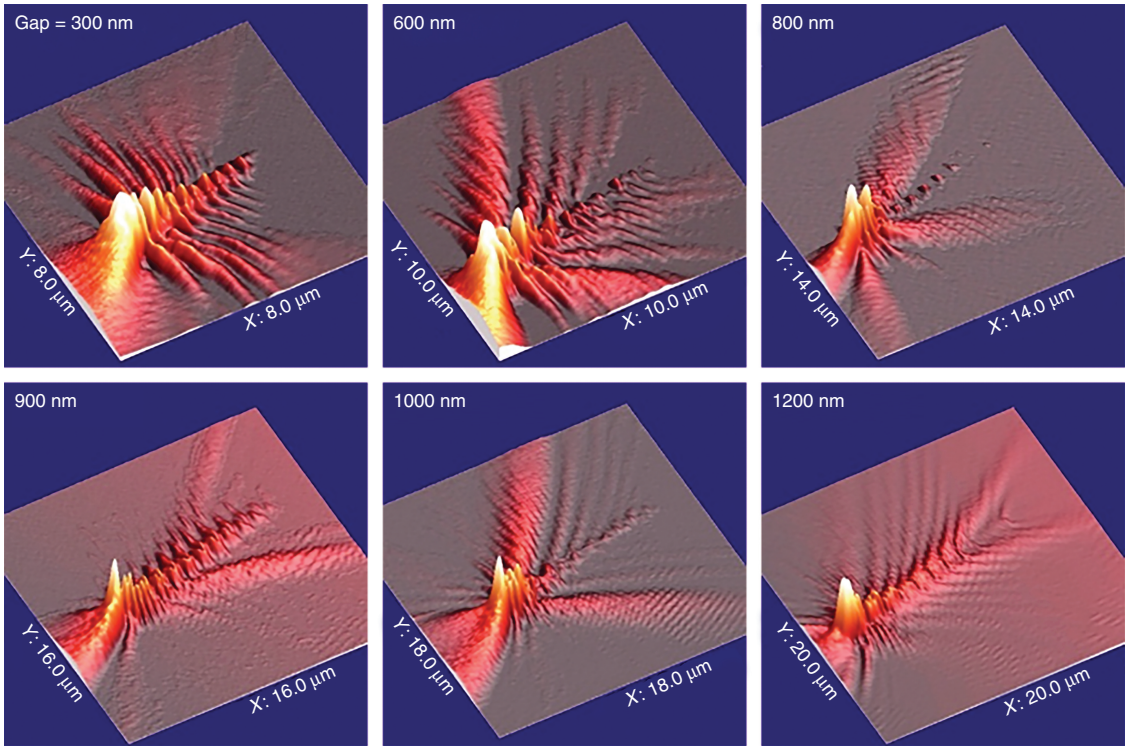

Figure 3 Near fields above the film, measured for different gaps when only the first cavity is excited. The excitation is produced using a linearly polarized He–Ne (632.8 nm) beam from the glass side, with polarization along the array long-axis to ensure plasmonic propagation along the array. The gap between the cavities is given in each panel.

time of the 'bottom' plasmon. The electric field at any point away from the array is given by:

$$\sum_{u=1}^{11}\sum_{v=-5}^{5}\sum_{w=-\frac{1}{2}}^{\frac{1}{2}} exp\left[\left(i\frac{2\pi}{\lambda_1}-L^{-1}\right)d(u,w)\right]E_{dipole}(\lambda_2,d,50v) \quad (1)$$

where E_{dipole} is the dipole radiation with a wavelength of λ_2, positioned at (d, 50v), u represents the running number of the hole in the array, v is the vertical position along each hole, w refers to the right or left side of the hole, λ_1 is the bottom plasmon wavelength, L is the plasmon decay length, and d is the distance between the source point and the first hole in the array such that:

$$d = (gap) * u + w * 100[nm] \quad (2)$$

where '*gap*' is the distance between the centers of two neighboring holes. As noted, the top and bottom plasmons propagate at different velocities. When only the top plasmon (gold–air) is included ($\lambda_1 = \lambda_2$), no wakes appear (Figure 2c). Similarly, no wakes are generated when only the bottom plasmon is calculated. However, wakes are generated (Figure 2d) when the phase of each source point is determined by the wavelength of the gold–glass plasmon, but the dipole radiation wavelength fits the gold–air plasmon. This case represents a physical situation where plasmons propagate at the gold–glass interface, and when they reach a nanocavity, they couple to localized surface plasmons (LSPs) at each cavity, which, in turn, couple to top propagating surface plasmons. Thus, it is the mismatch of the dipole's phase with its location that gives rise to the appearance of the wakes. Consequently, the wakes pattern varies with the change in the refractive index of the substrate, as demonstrated in the simulated results shown in Figure 5.

Near-field distributions using this dipole model were calculated for the different gaps, and the results for four different gaps are shown in Figure 6. The model describes the essence of the physical characteristics, but as explained earlier, the model is not expected to provide a quantitative fit to the observed or to the simulated results.

To further elucidate the contribution of the plasmon propagation on both sides of the film and to better understand the unique configuration resulting from the illumination of only a single hole, we considered the case of a first cavity that is blind, namely, light cannot pass from one side of the sample to the other. Figure 7 depicts the comparison between open and blind first cavities. For the case of a blind first cavity (shown at the inset), the plasmons on the gold–air side are generated at each hole by the excitation passing from below through the hole; thus, their phases are determined by the propagation delay on the gold–glass side. The wakes generated in the blind first hole configuration are essentially identical to the ones generated in the open first hole configuration (up to some intensity variations) but are shifted to the right by one hole. This observation strengthens the interpretation of the origin of the wakes and suggests that what we are seeing is the radiation from a phased array of plasmonic sources. In other words, the bottom (glass–gold) plasmon is responsible for the phase delay, and the propagating top plasmons originating from this phased array interfere, thus generating the wake configuration.

Based on the interference between the upper and lower propagating plasmons, any array of nanocavities in a metal film will generate wakes irrespective of their shape (circular, triangular and so on). The visibility and other details of these wakes depend on the geometry and shape of the individual cavities. We have tested various geometries and have mostly observed intensity differences stemming from the different scattering efficiencies of the different shapes (triangle, square or circle). As discussed, the physical mechanism leading to this effect is

 doi:10.1038/lsa.2017.72

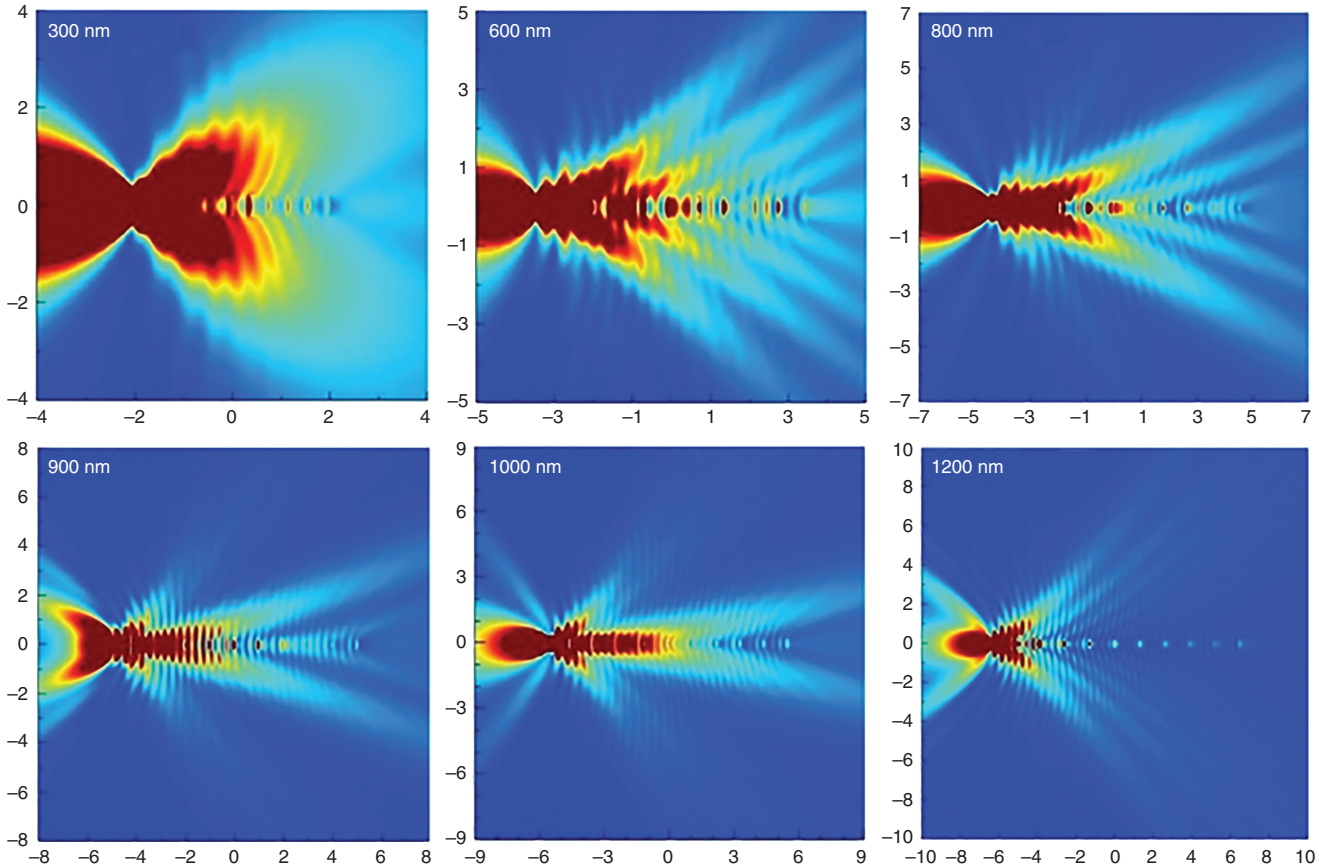

Figure 4 Calculated near fields above the film. Simulated near fields above the film for different gaps when only the first cavity is excited under the same conditions as in Figure 3.

the coupling between the upper and lower SPPs. Naturally, both SPPs should exist (that is, none has decayed), and the film thickness and cavity dimensions should be such that transmission through the cavity is possible.

Previously, Genevet *et al*[20]. reported the observation of plasmonic wakes from specially designed 1D rotated apertures in a gold film, under the excitation of a circularly polarized light beam at oblique incidence. The oblique incidence generates SPPs that propagate faster than the surface plasmon phase velocity, which interfere to form wakes the two-dimensional analog of Cherenkov radiation. In the current work, the different velocities on both sides of the film give rise to a phased array that is retarded when compared to the surface propagating plasmon at the gold–air interface, thus generating scattering from the phased antenna array that appears as wake fields. To control the wakes, one can choose the lattice constant of the array or the dielectric constant of the substrate, but these cannot be done interactively and require specific fabrication for each configuration. The potential approaches to dynamic control are presented below.

In general, wakes generated by a moving object are symmetric around the propagation direction. The same holds in the present case: the two-dimensional plasmonic wakes are observed to be distributed symmetrically on both sides of the cavity array. However, as we show below, it is possible to break the full symmetry by introducing asymmetry to the shape of the individual nanocavities. To test this possibility, we stamped a 'V'-shaped flaw into one side of each rectangular cavity in the array. The field distribution above the surface for a single imperfect rectangle was calculated numerically for various shapes, and indeed, the degree of asymmetry strongly depends on the geometry of the individual cavity. We determined that the best 'symmetry breaker' is a 'V'-shaped addition extending to a quarter of the total length of the rectangle. Figure 8a and 8b, depict the calculated and measured field distributions around a standard rectangle, and Figure 8c and 8d, depict the field around the asymmetrical one.

The measured and simulated near-field distributions around an array of these asymmetric cavities are shown in Figure 8e–8h, with clear asymmetry of the wake field around the array. The length of the 'V' shape is very crucial in making the wakes fully asymmetric with a zero field on one side. We determined that a blemish with a depth that is one quarter of the total length of the rectangle is optimal for maximal asymmetry. In most measurements, however, the asymmetry is less than perfect, and we attributed the residual field on the other side to fabrication imperfections due to the resolution-limited fabrication done via the FIB method.

The propagation of the SPP wakes is determined by the phases at the individual cavities along the array. As discussed, for a different refractive index of the substrate layer below the gold film, the propagation of the lower SPPs will be different, leading to a changed phased array of antennas and thus to an altered wake field. Moreover, different input wavelengths will yield different scattering patterns, providing another measure of control. This physical phenomenon leads to several potential applications, as detailed below.

Figure 9a depicts, in artificial color, the calculated wake field for different input wavelengths. In an array of 100×500 nm rectangular

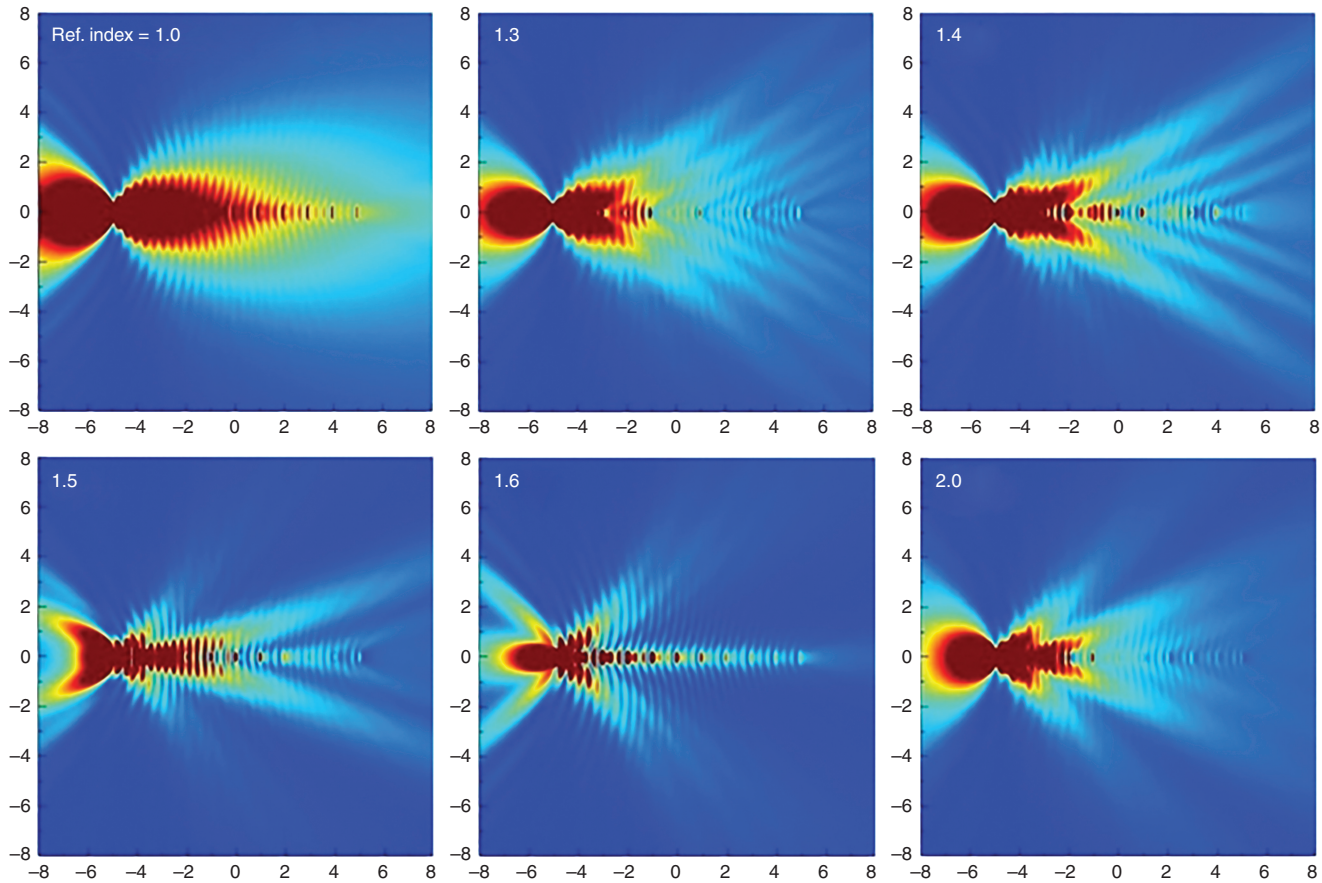

Figure 5 Dependence on substrate refractive index. Simulated near fields above an array with a 900 nm gap for a range of refractive indices.

cavities separated by 900 nm (marked in the panel), the first cavity is illuminated by a white light pulse, and the field above the gold film is plotted, where the plasmonic fields at 646 and 580 nm are colored red and green, respectively. The strong yellow region in the center is a result of both colors being present there. This configuration itself, without any further processing, may serve as an in-plane spectrum analyzer, alleviating the need for some distance propagation in the standard use of a grating for spectral analysis.

To simulate observations in the far field, we placed a small 'numerical detector' 1 μm above the gold film at point A (Figure 9a) and integrated the light intensity over the detector area. Figure 9b depicts the intensity of the far-field emission (as measured by the numerical detector) for substrate refractive indices of 1.5 and 1.6. The spectra in Figure 9b indicate a large variation in the plasmonic response as a function of the substrate refractive index (or, for that matter, of a cover layer), based on which the index can be extracted via far-field spectral measurements. To estimate the sensitivity of the device, we performed the following procedure for the analysis, as described in Figure 9c:

1. The emission ratio (at 646 and 580 nm) was numerically calculated for the 'unknown' substrate material (the value of 1.505 was arbitrarily selected).
2. Maps similar to Figure 9a were calculated over the range of 1.500–1.509, but at each pixel, 50% random noise was added.
3. The value of the 646 nm/580 nm ratio over observation area 'A' was calculated and was normalized to the value of the 'measured' (calculated) result at 1.505. Now, the goal is to see how accurately we can extract the value of 1.505 from the noisy calculations.
4. In Figure 9c, a horizontal line was drawn from 1 until it intersected the noisy curve, and then two vertical lines were drawn downward to identify the level of uncertainty of the derived index.
5. In the current example, the value of 1.505 ± 0.0004 is identified, providing an uncertainty level of 0.0004 in the determination of the refractive index of the unknown substrate.

CONCLUSIONS

We report the observation of plasmonic wake fields that are generated by the interference of two propagating plasmons with different velocities. The effect is observed for a gold film on a glass substrate and is based on the different effective refractive indices for SPP on the glass-side and the air-side of a metal film. The coupling between the top and bottom SPPs through the holes creates an array of phased antennas that causes the appearance of wake fields. The scattering of the wakes is not dependent on the illumination angle, and, in principle, the same mechanism should apply whenever two SPPs interfere. Owing to the strong dependence of the phases on the refractive index of the substrate, controlled change of this index will enable control of the directional propagation of the wake fields, opening options for directing, splitting and routing surface plasmons. A methodology is proposed for the determination of the substrate index of refraction with high accuracy. Several proposals for controlled refractive index changes have been published in recent years[32–38], and further experiments are underway to utilize these proposals.

doi:10.1038/lsa.2017.72

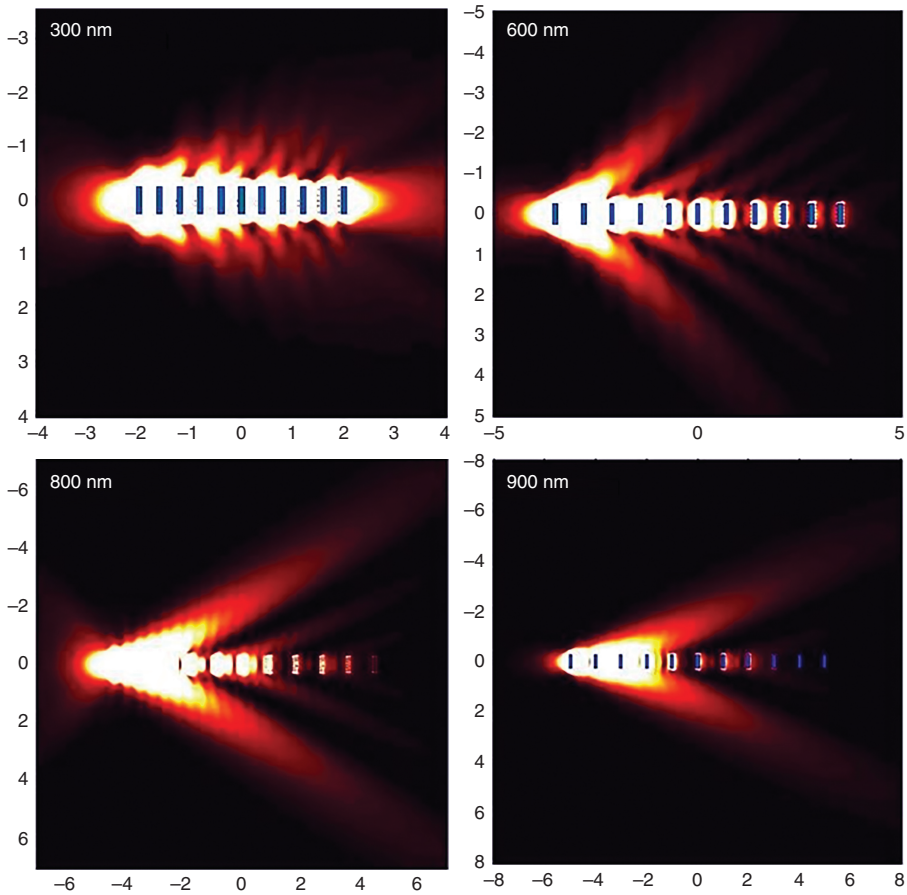

Figure 6 Model calculations. Calculated electric field above the gold film, with many dipoles around each nanocavity location. The laser illumination (632.8 nm) from below is focused on the left-most cavity.

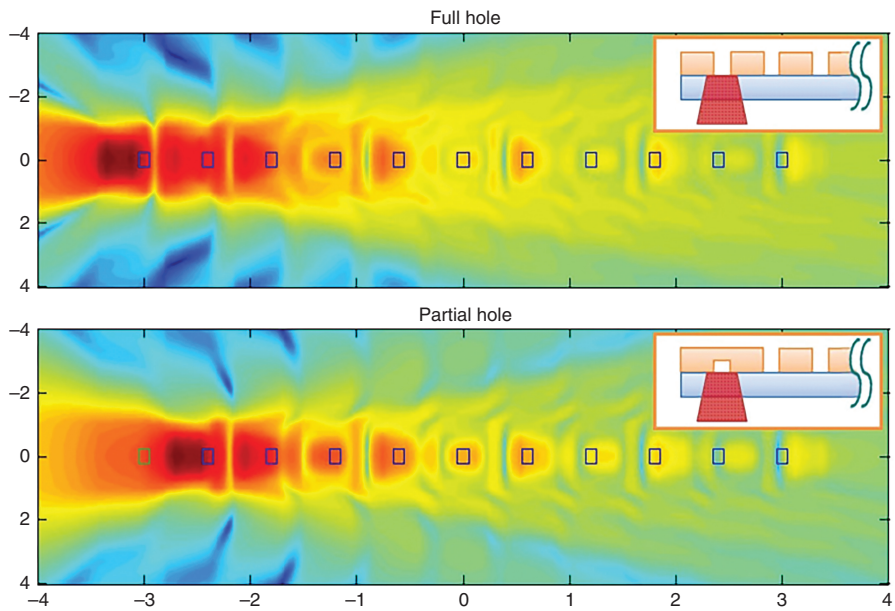

Figure 7 Open and blind first cavities. The near fields above the array with a gap of 500 nm are depicted for two cases: for an open first hole (upper) and for a blind first hole (lower). The insets portray the geometry of the two configurations. As shown, the field distributions are quite similar but shifted to the right for the blind hole.

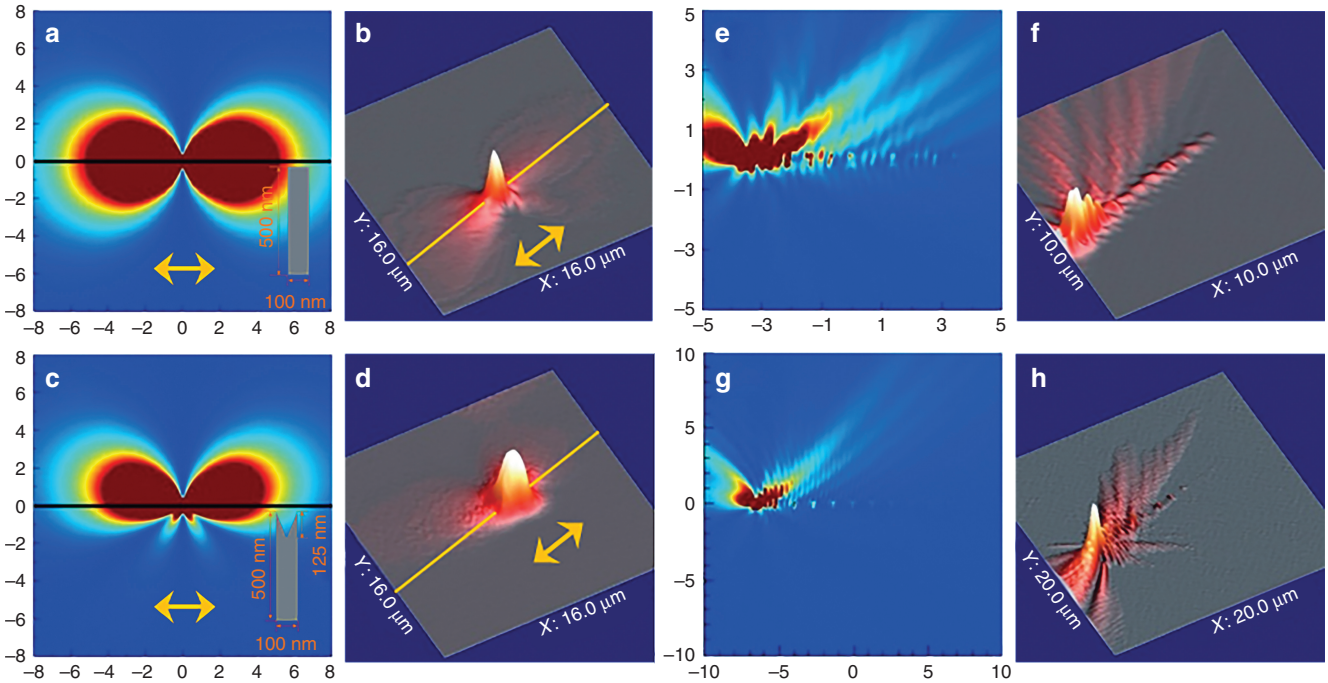

Figure 8 Asymmetric wakes. (**a**) and (**b**) Simulated and measured near-field distribution above a single rectangle; (**c**) and (**d**) simulated and measured near-field distribution of a single asymmetric rectangle; (**e**) and (**f**) simulated and measured asymmetric wakes for an array with a gap of 600 nm; (**g**) and (**h**) the same, but with a gap of 1200 nm. Yellow arrows indicate the direction of polarization, whereas the black and yellow lines pass through the center of the rectangle.

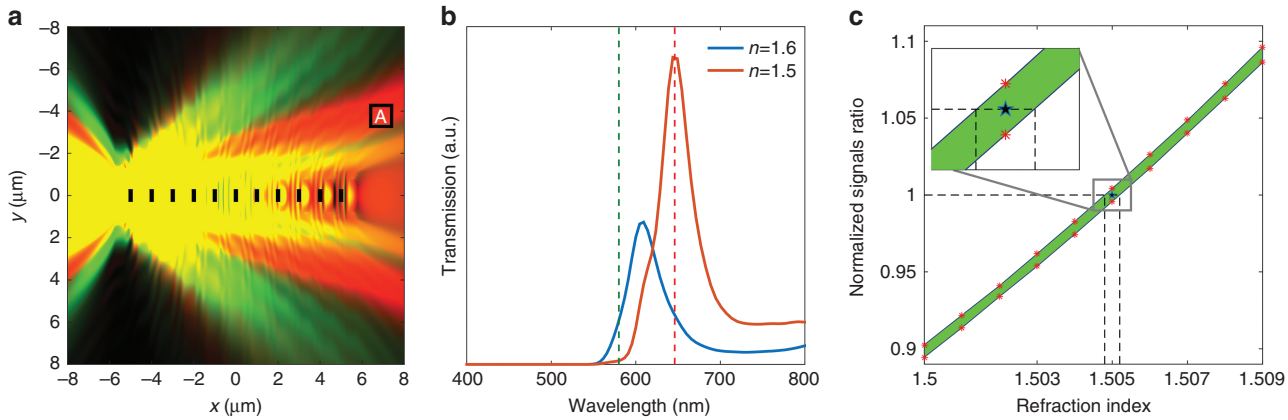

Figure 9 Refractive index effects. (**a**) Calculated near-field map of the wake field above an array of 100 × 500 nm rectangular cavities separated by 900 nm in a gold film of thickness 350 nm following excitation of the first cavity by a white light pulse. The fields at 646 and 580 nm were artificially colored red and green, respectively. (**b**) Intensity spectrum as observed by a numerical detector positioned at point 'A' for substrate refractive indices of 1.5 (blue) and 1.6 (brown). (**c**) For a range of values of the refractive index from 1.500 to 1.509, the ratio was extracted from the corresponding maps after 50% random noise was added to each pixel. The calculated results were compared to the 'nominally measured' result (also numerically calculated), from which the value of the substrate refractive index was found to be $n = 1.505 \pm 0.0004$. See text for details.

CONFLICT OF INTEREST

The authors declare no conflict of interest.

ACKNOWLEDGEMENTS

Useful discussions with Euclides Almeida and Guy Shalem are gratefully acknowledged. This work was supported by the Israel Science Foundation grant no. 1242/12, by the ICORE program, by an FTA grant from the Israel National Nano Initiative and by the Minerva Foundation.

1 Radko IP, Bozhevolnyi SI, Brucoli G, Martín-Moreno L, García-Vidal FJ *et al.* Efficient unidirectional ridge excitation of surface plasmons. *Opt Express* 2009; **17**: 7228–7232.
2 López-Tejeira F, Rodrigo SG, Martín-Moreno L, García-Vidal FJ, Devaux E *et al.* Efficient unidirectional nanoslit couplers for surface plasmons. *Nat Phys* 2007; **3**: 324–328.
3 Huang XP, Brongersma ML. Compact aperiodic metallic groove arrays for unidirectional launching of surface plasmons. *Nano Lett* 2013; **13**: 5420–5424.
4 Baron A, Devaux E, Rodier JC, Hugonin JP, Rousseau E *et al.* Compact antenna for efficient and unidirectional launching and decoupling of surface plasmons. *Nano Lett* 2011; **11**: 4207–4212.

5 Chen JJ, Li Z, Yue S, Gong QH. Efficient unidirectional generation of surface plasmon polaritons with asymmetric single-nanoslit. *Appl Phys Lett* 2010; **97**: 041113.
6 Li DD, Zhang DH, Yan CC, Li T, Wang YK *et al.* Unidirectional surface plasmon-polariton excitation by a compact slot partially filled with dielectric. *Opt Express* 2013; **21**: 5949–5956.
7 Wang L, Li T, Li L, Xia W, Xu XG *et al.* Electrically generated unidirectional surface plasmon source. *Opt Express* 2012; **20**: 8710–8717.
8 Lerosey G, Pile DFP, Matheu P, Bartal G, Zhang X. Controlling the phase and amplitude of plasmon sources at a subwavelength scale. *Nano Lett* 2009; **9**: 327–331.
9 Braun KF. *Electrical Oscillations and Wireless Telegraphy.* Nobel Lecture: Stockholm, 1909.
10 Capmany J, Novak D. Microwave photonics combines two worlds. *Nat Photonics* 2007; **1**: 319–330.
11 Sun J, Timurdogan E, Yaacobi A, Hosseini ES, Watts MR. Large-scale nanophotonic phased array. *Nature* 2013; **493**: 195–199.
12 DeRose CT, Kekatpure RD, Trotter DC, Starbuck A, Wendt JR *et al.* Electronically controlled optical beam-steering by an active phased array of metallic nanoantennas. *Opt Express* 2013; **21**: 5198–5208.
13 Liu YM, Palomba S, Park Y, Zentgraf T, Yin XB *et al.* Compact magnetic antennas for directional excitation of surface plasmons. *Nano Lett* 2012; **12**: 4853–4858.
14 Lin J, Mueller JPB, Wang Q, Yuan GH, Antoniou N *et al.* Polarization-controlled tunable directional coupling of surface plasmon polaritons. *Science* 2013; **340**: 331–334.
15 Yin LL, Vlasko-Vlasov VK, Pearson J, Hiller JM, Hua J *et al.* Subwavelength focusing and guiding of surface plasmons. *Nano Lett* 2005; **5**: 1399–1402.
16 Minovich A, Klein AE, Janunts N, Pertsch T, Neshev DN *et al.* Generation and near-field imaging of airy surface plasmons. *Phys Rev Lett* 2011; **107**: 116802.
17 Yu NF, Genevet P, Aieta F, Kats MA, Blanchard RG *et al.* Flat optics: controlling wavefronts with optical antenna metasurfaces. *IEEE J Sel Top Quant Electron* 2013; **19**: 4700423.
18 Yu NF, Genevet P, Kats MA, Aieta F, Tetienne JP *et al.* Light propagation with phase discontinuities: generalized laws of reflection and refraction. *Science* 2011; **334**: 333–337.
19 Almeida E, Shalem G, Prior Y. Subwavelength nonlinear phase control and anomalous phase matching in plasmonic metasurfaces. *Nat Commun* 2016; **7**: 10367.
20 Genevet P, Wintz D, Ambrosio A, She A, Blanchard R *et al.* Controlled steering of Cherenkov surface plasmon wakes with a one-dimensional metamaterial. *Nat Nanotechnol* 2015; **10**: 804–809.
21 Smith SJ, Purcell EM. Visible light from localized surface charges moving across a grating. *Phys Rev* 1953; **92**: 1069.
22 Luo CY, Ibanescu M, Johnson SG, Joannopoulos JD. Cerenkov radiation in photonic crystals. *Science* 2003; **299**: 368–371.
23 Chuang SL, Kong JA. Enhancement of smith-purcell radiation from a grating with surface-plasmon excitation. *J Opt Soc Am A* 1984; **1**: 672–676.
24 Salomon A, Prior Y, Fedoruk M, Feldmann J, Kolkowski R *et al.* Plasmonic coupling between metallic nanocavities. *J Opt* 2014; **16**: 114012.
25 Fu YL, Hu XY, Lu CC, Yue S, Yang H *et al.* All-optical logic gates based on nanoscale plasmonic slot waveguides. *Nano Lett* 2012; **12**: 5784–5790.
26 Chen YG, Chen YH, Li ZY. Direct method to control surface plasmon polaritons on metal surfaces. *Opt Lett* 2014; **39**: 339–342.
27 Kabakova IV, de Hoogh A, van der Wel REC, Wulf M, le Feber B *et al.* Imaging of electric and magnetic fields near plasmonic nanowires. *Sci Rep* 2016; **6**: 22665.
28 Kawata S, Inouye Y, Verma P. Plasmonics for near-field nano-imaging and superlensing. *Nat Photonics* 2009; **3**: 388–394.
29 Lumerical Solutions, Inc. 2014. http://www.lumerical.com/tcad-products/fdtd.
30 Johnson PB, Christy RW. Optical constants of the noble metals. *Phys Rev B* 1972; **6**: 4370–4379.
31 Palik ED. *Handbook of Optical Constants of Solids*. San Diego, California: Academic Press, 1998.
32 Feigenbaum E, Diest K, Atwater HA. Unity-order index change in transparent conducting oxides at visible frequencies. *Nano Lett* 2010; **10**: 2111–2116.
33 Milton HE, Nagaraj M, Kaur S, Jones JC, Morgan PB *et al.* Field-induced refractive index variation in the dark conglomerate phase for polarization-independent switchable liquid crystal lenses. *Appl Optics* 2014; **53**: 7278–7284.
34 Yan J, Jiao MZ, Rao LH, Wu ST. Direct measurement of electric-field-induced birefringence in a polymer-stabilized blue-phase liquid crystal composite. *Opt Express* 2010; **18**: 11450–11455.
35 Reed GT, Png CEJ. Silicon optical modulators. *Mater Today* 2005; **8**: 40–50.
36 Aitchison JS, Weiner AM, Silberberg Y, Oliver MK, Jackel JL *et al.* Observation of spatial optical solitons in a nonlinear glass waveguide. *Opt Lett* 1990; **15**: 471–473.
37 Valley GC, Segev M, Crosignani B, Yariv A, Fejer MM *et al.* Dark and bright photovoltaic spatial solitons. *Phys Rev A* 1994; **50**: R4457–R4460.
38 Nikolajsen T, Leosson K, Bozhevolnyi SI. Surface plasmon polariton based modulators and switches operating at telecom wavelengths. *Appl Phys Lett* 2004; **85**: 5833–5835.

This work is licensed under a Creative Commons Attribution-NonCommercial-NoDerivs 4.0 International License. The images or other third party material in this article are included in the article's Creative Commons license, unless indicated otherwise in the credit line; if the material is not included under the Creative Commons license, users will need to obtain permission from the license holder to reproduce the material. To view a copy of this license, visit http://creativecommons.org/licenses/by-nc-nd/4.0/

© The Author(s) 2017